This article has been accepted for publication in IEEE Transactions on Terahertz Science and Technology. This is the author's version which has not been fully edited and content may change prior to final publication. Citation information: DOI 10.1109/TTHZ.2023.3275270

Observation of topological transmission in terahertz domino waveguide array

Pan Hu, Lin Chen, *Member IEEE*, Alexander P. Shkurinov, Yiming Zhu, *Senior member IEEE*, and Songlin Zhuang

***Abstract*—In this paper, we propose on-chip terahertz domino waveguide array structures which can enable the topological effect and enhance the robustness of terahertz transmission. Terahertz topological effect (include topologically-protected edge states and binding states) is excited by constructing kink and antikink structures in designed domino waveguide arrays. Furthermore, the robustness of topological waveguide arrays is successfully demonstrated. The topological transmission effects have been experimentally demonstrated using scanning near-field terahertz microscopy. Our study provides a new approach to study the topological photonic transport of waveguide arrays in the terahertz regime and has potential application in terahertz integrated circuit.**

***Index Term*—Terahertz, domino plasmons, topological photonics, waveguide array**

I. Introduction

Terahertz (THz) waves are located between microwave and infrared waves (0.1 THz - 10 THz) [1-3]. They show some unique characteristics such as fingerprint spectrum identification [4], nondestructive detection [5], and broadband 6G communication [6], and thus, have recently paid much more attention for both mechanisms and applications. However, most THz systems are composed of bulky and discrete components, including coupler, beam splitter, waveguides, and lenses [7-12]. An on-chip integration platform is required to reduce size of the components. This on-chip integration platform is also defined as THz integrated circuit (IC) [13-15], which is indispensable towards the practical use in various fields. The low-loss waveguides on chip are the most fundamental and key components for the development of THz ICs. Various waveguides on a thin planar platform had been fully discussed, such as transmission line [16-18] and silicon photonic crystals (PC) [19-21]. THz transmission lines are one-dimensional (1D) transmission waveguide and can be easily fabricated by conventional electronics and photonics technologies, but they suffered from large ohmic loss induced by metals at terahertz frequencies. Silicon PC slabs consisting of a two-dimensional (2D) lattice of air holes demonstrates the strong electromagnetic confinement due to existence of photonic bandgap (PBG). Such PC waveguides and silicon waveguides using total internal reflections [22-26] can also realize a low-loss waveguide because the silicon absorption can be managed by controlling the doped carrier density. They have several advantages: (1) modal fields can be confined into a subwavelength-width core; (2) it is proved to be compact, for instance, the lateral periodicity of the PC is about 25% of a free-space wavelength at about 0.3 THz [19]; (3) it is monolithic because the entire structure is fabricated from a single silicon wafer; (4) it is versatile and can integrate various functions such as frequency-division multiplexer [20], antenna array [21], topological on chip communication [27], etc. We noticed that the THz wave was commonly coupled into PC waveguides by hollow metallic waveguide and tapered structure. And PC waveguides were measured by using a continuous wave (CW) electronic source, which was produced by combining a millimeter-wave signal generator & multiplier and showed limited bandwidth (for instance, 0.28–0.39 THz range in Ref.[19]). To cover wideband frequency range (for instance, 0.1-1.5THz), double or triple frequency conversion should be prepared. Typical tripler conversion efficiency of multiplier is low (1.5% for output frequency range 0.5-0.75 THz and 0.1-0.7% for output frequency range 1.1-1.6 THz) [28], resulting in low output power. Meanwhile, broadband THz TDS system is widely used in THz field. Therefore, exploring alternative robust THz waveguides in combination with broadband THz TDS system is necessary to achieve THz IC with selected operation frequency.

Domino waveguide, which consists of a chain of periodic metallic domino-like pieces on top of a metallic surface [29], is an excellent candidate for the building of compact THz ICs. Domino waveguides have the same features as PC waveguides: (1) it carries subwavelength transverse cross section localization; (2) it is planar, monolithic and easily manufactured; (3) it is versatile for the design of key functional devices with small absorption and bend losses [30]. The flexibility and

This work was supported in part by the Basic Science Center Project of the National Natural Science Foundation of China (Grant No. 61988102), National Natural Science Foundation of China (grant no. 62275157), the Shanghai Shuguang Program, China (Grant No. 18SG44), 111 Project (grant no. D18014). We thank professor Qingqing Cheng of University of Shanghai for Science and Technology for his theoretical guidance and associate professor Yanfeng Li and Dr. Mingrui Yuan of Tianjin University for their experimental guidance.(Corresponding author:Lin Chen)

P. Hu, Y. Zhu, S. Zhuang, and L. Chen, are with Shanghai Key Lab of Modern Optical System, University of Shanghai for Science and Technology, Shanghai 200093, People's Republic of China. (e-mail: linchen@usst.edu.cn)

L. Chen is also with Shanghai Institute of Intelligent Science and Technology, Tongji University, Shanghai 200092, People's Republic of China.

Alexander. P. Shkurinov are with Faculty of Physics and International Laser Center, Lomonosov Moscow State University, Moscow 119991, Russia

ORCID: Lin CHEN, http://orcid.org/0000-0002-6848-5257

Authorized licensed use limited to: University of Shanghai For Science and Technology. Downloaded on May 21,2023 at 03:15:13 UTC from IEEE Xplore. Restrictions apply.
© 2023 IEEE. Personal use is permitted, but republication/redistribution requires IEEE permission. See https://www.ieee.org/publications/rights/index.html for more information.

This article has been accepted for publication in IEEE Transactions on Terahertz Science and Technology. This is the author's version which has not been fully edited and content may change prior to final publication. Citation information: DOI 10.1109/TTHZ.2023.3275270

versatility of domino waveguides had already been demonstrated through the implementation of a variety of functional devices, such as THz coupler [31], switch [32], beam splitter [30], wavelength division multiplexing [33] and logic gate structure devices [34]. More importantly, the THz wave can be coupled into domino waveguides by integrated with tapered grating on a single silicon wafer. And domino waveguides can be successfully measured by using a THz scanning near-field terahertz microscopy with a broadband photoconductive emission antenna and a probe [30]. In this work, the THz domino waveguides array is fully investigated to further expand applications of domino platform. To the best of our knowledge, it is the first time that the THz topological transport has been implemented on the coupled domino waveguides array [29]. First, we analyze the dispersion properties of two domino waveguides and the coupling properties between two waveguides. Then, we develop the Su-Schrieffer-Heeger (SSH) model [35-38] for the domino waveguides array structure, and derive the Hamiltonian matrix by coupling mode theory and the Schrödinger equation. Third, by using the domino waveguide array parameters and designing the kink and antikink structures [39], we have successfully excited the THz topologically-protected edge states and binding states and verified the robustness of both topologies by introducing structural deviation degree. The topological transmission of our domino platform has a significant role in both foundation and application. Fundamentally, the domino waveguides array provides macroscopic THz platform analogues of such important quantum phenomena (the topological phases) in the condensed matters without requiring special synthetic media with subwavelength controllability. In application, our work realized that the topological protection is introduced into THz IC, which can enhance the robustness of THz signal integrity with defects and disorders, i.e., significant features in THz communications [13-15].

II. Design of THz One-Dimensional Topological Photonic Chip

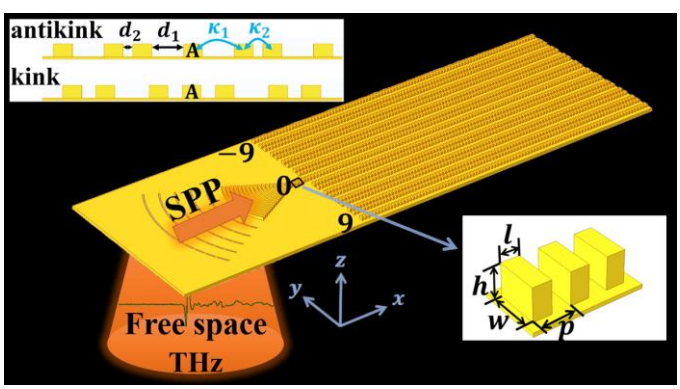

Fig. 1. The schematic of implementing THz topologically-protected edge states in the 1D domino waveguide array. The upper left inset is the antikink and kink structures [*d* (*d*₁ and *d*₂) represents the waveguide spacing, *κ* (*κ*₁ and *κ*₂) is the coupling coefficient between the waveguides, and A represents the central waveguide of the input energy]. The lower right inset is detailed domino waveguide structure, where *w* = 120 μm, *p* = 100 μm, *h* = 80 μm, and *l* = 50 μm. We number the waveguide array along the *y*-axis from positive to negative direction as -9…9.

Figure 1 shows a schematic of implementing topological effect in THz 1D domino waveguide array. The structure is divided into three parts: the excitation region, the energy focus region and the energy transmission region. THz spoof surface plasmonic polariton (SSPP) [40-44] are excited by the curved holes array. The excited domino plasmon is focused through periodic-decreasing fan funnel waveguides and finally transmitted through the transmission region. The upper left inset of Fig. 1 is the design of the antikink and kink structures. The single domino waveguide structure is shown in the lower right inset of Fig. 1.

We choose the parameters of the single domino structure as w = 120 μm, p = 100 μm, h = 80 μm, and l = 50 μm. The eigenmode solver of the commercial software CST Microwave Studio is used to analyze the dispersion curves of the odd mode (k_{ssppo}) and even mode (k_{ssppe}) with different waveguide spacing d, as shown in Fig. 2(a). Based on the equation $k_{sspp} = \theta * \pi / (180 * p)$, the values of k_{sspp} were obtained, where θ is variation in x direction. Here, the k_{sspp} is equivalent to the propagation constant β in the waveguide.

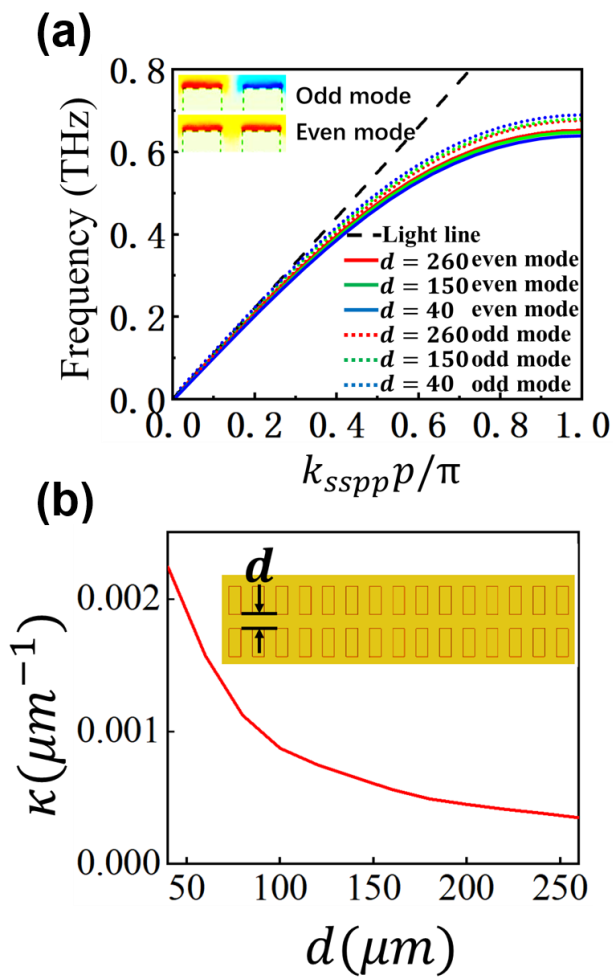

Fig. 2. (a) Dispersion relation of odd and even modes for waveguides with varying *d*. The upper left inset shows the normalized electric field distribution of the two modes with

Authorized licensed use limited to: University of Shanghai For Science and Technology. Downloaded on May 21,2023 at 03:15:13 UTC from IEEE Xplore. Restrictions apply.
© 2023 IEEE. Personal use is permitted, but republication/redistribution requires IEEE permission. See https://www.ieee.org/publications/rights/index.html for more information.

This article has been accepted for publication in IEEE Transactions on Terahertz Science and Technology. This is the author's version which has not been fully edited and content may change prior to final publication. Citation information: DOI 10.1109/TTHZ.2023.3275270

d = 60 μm at 0.5 THz. (b) The coupling coefficients κ as a function of gap d.

Within the first Brillouin zone, the k_{sspp} of the domino waveguide mode became larger than the light line (black dotted line) with increasing frequency, which means that the surface with pillars possesses good field confinement ability. For the odd mode, the cut-off frequency increases with the increase of d. For the even mode, the cut-off frequency decreases with the increase of d. The upper left inset of Fig. 2(a) shows the normalized electric field distribution of the two modes with d = 60 μm at 0.5 THz. To obtain the relation between the different waveguide spacing d and the coupling coefficients κ, we use the supermode theory to analyze. The difference of the propagation constants k_{sspp} for two supermodes causes the phase difference. When the phase difference reaches π, the energy is coupled from one waveguide to another, with its length called L_c. The relationship between coupling length L_c and the coupling coefficients κ is $\kappa L_c = \pi / 2$, where $\kappa = (k_{ssppe} - k_{ssppo}) / 2$. We also plot the relationship between waveguide spacing d and the coupling coefficient κ, as shown in Fig. 2(b). By using the supermode theory, it can be found that the coupling coefficient decreases with the increasing waveguide spacing. These results will be used in the following THz topological domino waveguide design.

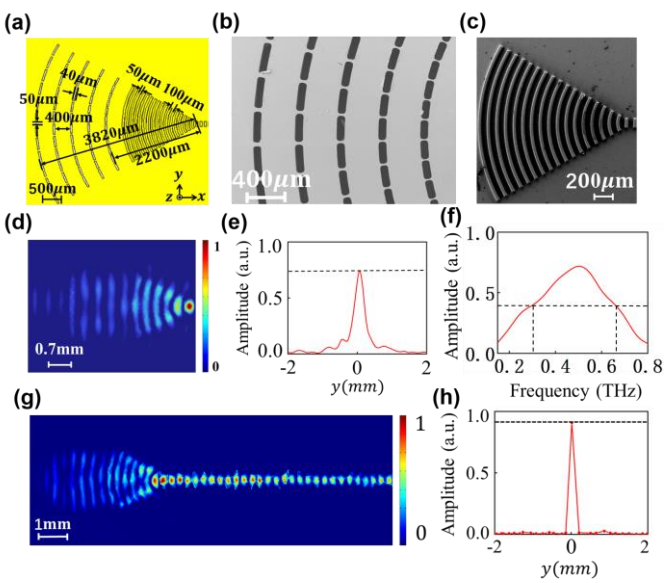

Fig. 3. (a) The schematic of the coupling and focused regions. (b-c) The SEM image of the fabricated arc-shaped curved hole array excitation region as well as the fan-shaped coupling region. (d) The simulated electric field distribution of (a). (e) Amplitude of the electric field at 0.5 THz for the output port of coupling region in (a). (f) Amplitude at output port of coupling region as a function of operation frequency. (g)The electric field distributions at 0.5 THz corresponding to the single root waveguide. (h) Output port amplitude distribution for the single domino waveguide.

THz wave is commonly coupled into the PC waveguides from the waveguide port by employing the near-field coupling techniques [19]. However, such near-field coupling techniques can't be employed into the domino waveguide due to the momentum mismatch between free-space THz wave vector and domino surface plasmons wave vector. The methods on excitation of THz domino surface plasmons that can achieve the momentum match are generally based on prism coupling or grating coupling [45]. Compared to prism coupling which the existence of bulk prism doesn't benefit to integration, the grating coupling with a gradually reduced width next to the grating can convert more free-space THz waves to domino surface plasmons at the on-chip integration platform without any bulk prism usage.

The excited domino plasmon are coupled to the waveguide through a fan funnel consisted of a period-reduced column. Both the excited hole arrays and a funnel-shaped array of metal columns have the ability to focus the energy on a strong point with a subwavelength width. The schematic of the arc-shaped curved hole array excitation and the fan-shaped coupling region, as well as the scanning electron microscopy (SEM) image consisting coupling and focusing regions, as shown in Figure 3(a-c). The radii of the innermost and outermost layers of the curved hole array are 2220 μm and 3820 μm, respectively. The width of each hole array is 40 μm, the period along the radial direction is 400 μm and the center corner of the curved hole is 60°. The curved hole arrays are divided into smaller holes by metal strips with a spacing of 50 μm and a center angle of 5°. The radial period between the arc waveguides is 100 μm, and each array width is 50 μm. To evaluate the coupling efficiency of the grating coupler, we numerically obtained the output electric field amplitude of the waveguide at the end of the coupling region at 0.5 THz, as shown in Fig. 3 (d)-(e). The coupling efficiency is about 73% at 0.5 THz. We also obtained the coupling efficiency of the grating coupler with respect to operation frequency, as shown in Fig. 3(f). At broadband frequency range 0.3-0.66 THz, the coupling efficiency of the grating coupler can achieve larger than 40%.

To verify the focusing power of this structure, we simulated the electric field distribution of a single domino waveguide, as shown in Fig. 3(g). The results demonstrate that the electric field is well focused on the single domino waveguide, which is also clearly proved by the output port amplitude distribution in Fig. 3(h) (normalized by input port amplitude at output port of coupling region).

The above result in Fig. 3(h) neglects actual metallic loss in simulation. Actually, a thin gold film was coated on the silicon wafer. So the ohmic loss of the metal should be taken into account. For single domino waveguide (Fig. 4(a)), Figure 4(b) shows the propagation length l as a function of operation wavelength by considering the ohmic loss of the metal. Here $l = (2\mathrm{Im}(k))^{-1}$, where Im (k) is the imaginary part of propagation constant of domino surface plasmons. As operation wavelength increases from cutoff wavelength (0.47mm), propagation length increases and the dispersion curve approaches the light line. For λ = 0.6 mm (0.5 THz), h = 0.8p, w = 1.2p, and p = 100 μm, the propagation length is about 20λ or 12mm when amplitude reduces to 0.368 (1/e). The propagation length is larger than the size of the chips in this work. The simulated power propagation losses of the single straight waveguide is only about 0.46 dB/mm. In the following section we gave the lossless results by setting metal as perfect electric conductor to better exhibit the topological protected edge states. Meanwhile,

Authorized licensed use limited to: University of Shanghai For Science and Technology. Downloaded on May 21,2023 at 03:15:13 UTC from IEEE Xplore. Restrictions apply.
© 2023 IEEE. Personal use is permitted, but republication/redistribution requires IEEE permission. See https://www.ieee.org/publications/rights/index.html for more information.

This article has been accepted for publication in IEEE Transactions on Terahertz Science and Technology. This is the author's version which has not been fully edited and content may change prior to final publication. Citation information: DOI 10.1109/TTHZ.2023.3275270

the transmittance and propagation loss of all the results have also been pointed out by considering ohmic loss.

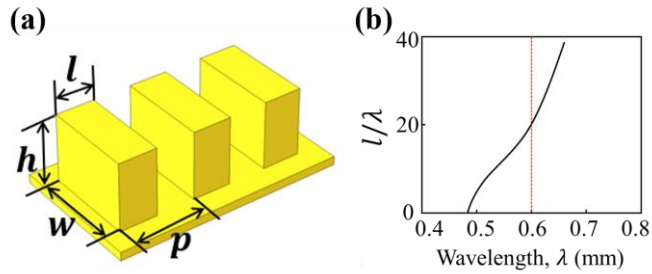

Fig. 4 (a) The schematic of the single domino waveguide structure with the following geometrical parameters: the period *p*, the width *w*, the length *l*, and the depth *h* of the pillar. (b) Normalized propagation length (*l*/λ) induced by ohmic loss as a function of λ (h = 0.8p, w = 1.2p, p = 100 μm).

We also measured the amplitude along the single domino waveguide in *x* direction with the step of 0.2 mm. The normalized results with input amplitude are shown in Fig. 5. Then we gave an exponential fit for the results to avoid the measured amplitude fluctuation. The correlation coefficient R^2 can achieve 0.95685. The amplitude in fitting curve at 1 mm position is 0.909. Then the power amplitude is 0.826. So the corresponding power propagation loss was about 0.83 dB/mm, which is close to the power propagation loss 0.8 dB/mm in Ref. [30]. Detailed description about propagation losses of various THz waveguides can be found in Supplementary material [46].

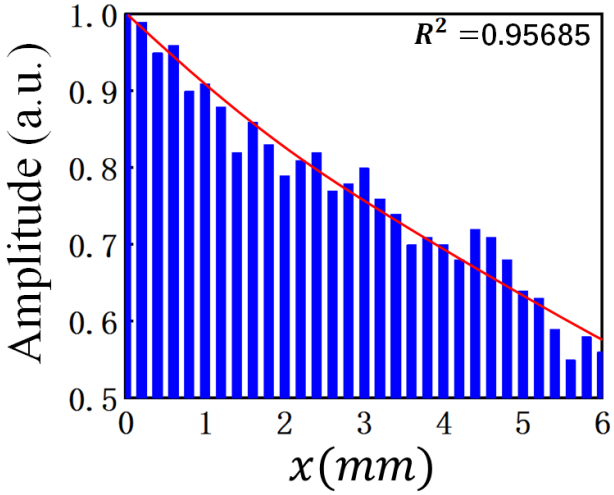

Fig. 5 Amplitude attenuation as a function of propagation distance. Blue pillar represents measured results, and the solid red line is the exponential fit.

III. THE KINK AND ANTIKINK STRUCTURES

The SSH model is the simplest two band model for polyacetylene, and it has a chiral symmetry. Both topological trivial phase and topological non-trivial phase are supported in this dimer chain. By combining the trivial and non-trivial phases together, the topological phase transition interfaces can be formed. There are also two different forms of the interface, depending on the different way of the combination. When the two lattices are connected through a weaker coupling κ_1, they are called the antikink interface. In contrast, when the two lattices are connected by a strong coupling κ_2, it is called the kink interface, as shown in the upper left inset of Figure 1 (A represents the central waveguide and *d* is the waveguide spacing). If the domino plasmon is coupled from the center A waveguide, it will match the mode distribution of the topologically-protected edge states. Detailed description about the SSH model for the domino waveguide dimer chains in one dimension can be found in Supplementary material [46].

We analyzed the propagation of the domino plasmon in the THz domino topologic array by using the coupled-mode theory (CMT) in the tight-bound approximation (TBA). Analogous to the TBA model, the propagation of domino plasmon can be described by [32-33]:

$$-i\frac{\partial}{\partial x}a_n = \beta_n a_n + \kappa_{n.n+1}a_{n+1} + \kappa_{n.n-1}a_{n-1} \tag{1}$$

Where a_n is the amplitude in the *n*th domino waveguide (here $n = -9, -8, \ldots, 8, 9$, total waveguide number is N = 19), β_n is the propagation constant of the waveguide.

The electromagnetic waves propagate can be expressed by the Schrödinger equation ($i\hbar\frac{\partial}{\partial t}\psi = H\psi$), we can write the CMT in the form of Schrodinger-like equation:

$$i\frac{\partial}{\partial x}a_n = Ha_n \tag{2}$$

Based on equation (1) and equation (2), the Hamiltonian of the kink and antikink structures can be written as a matrix form, where the subscript 19×19 of the matrix refers to the 19 waveguides. These matrices are used in the following mode diagram analysis.

$$H_{antikink} = \begin{bmatrix} \beta & \kappa_1 & & & & & & & \\ \kappa_1 & \beta & \kappa_2 & & & & & & \\ & \kappa_2 & O & O & & & & & \\ & & O & \beta & \kappa_1 & & & & \\ & & & \kappa_1 & \beta & \kappa_1 & & & \\ & & & & \kappa_1 & \beta & O & & \\ & & & & & O & O & \kappa_2 & \\ & & & & & & \kappa_2 & \beta & \kappa_1 \\ & & & & & & & \kappa_1 & \beta \end{bmatrix}_{19\times19} \tag{3}$$

$$H_{kink} = \begin{bmatrix} \beta & \kappa_2 & & & & & & & \\ \kappa_2 & \beta & \kappa_1 & & & & & & \\ & \kappa_1 & O & O & & & & & \\ & & O & \beta & \kappa_2 & & & & \\ & & & \kappa_2 & \beta & \kappa_2 & & & \\ & & & & \kappa_2 & \beta & O & & \\ & & & & & O & O & \kappa_1 & \\ & & & & & & \kappa_1 & \beta & \kappa_2 \\ & & & & & & & \kappa_2 & \beta \end{bmatrix}_{19\times19} \tag{4}$$

For the antikink structure, we chose d_1 = 200 μm and d_2 = 60 μm as the separation distances between waveguides, the corresponding coupling coefficients are κ_1 = 0.000449 μm^{-1} and

Authorized licensed use limited to: University of Shanghai For Science and Technology. Downloaded on May 21,2023 at 03:15:13 UTC from IEEE Xplore. Restrictions apply.
© 2023 IEEE. Personal use is permitted, but republication/redistribution requires IEEE permission. See https://www.ieee.org/publications/rights/index.html for more information.

This article has been accepted for publication in IEEE Transactions on Terahertz Science and Technology. This is the author's version which has not been fully edited and content may change prior to final publication. Citation information: DOI 10.1109/TTHZ.2023.3275270

$\kappa_2 = 0.001571$ μm^{-1}. For the single domino waveguide, we chose propagation constant of $\beta = 0.017$ μm^{-1}. For the kink structure, we chose d_1 = 220 μm and d_2 = 90 μm as the separation distances between waveguides, the corresponding coupling coefficients are $\kappa_1 = 0.000413$ μm^{-1} and $\kappa_1 = 0.000998$ μm^{-1}. By calculating the eigenvalues of the equation (3) and (4), we can obtain the mode diagram. The transverse propagation constant of this topological structure is zero, which implies that the mode will remain exponentially localized at the interface.

For the antikink structure with 19 waveguides, it is clearly observed that the band structure has the characteristics of band gap separation, and three topological defect modes appear in the center of the energy band, as shown in Fig. 6(a), where the topological defect modes are framed by boxes. We analyze the edge modes formed by these three topological defect modes as one central interface mode and two edge waveguides, respectively. To verify this, we calculated the band diagram for 17 waveguides. It can be seen that the center of the energy band is only a topological defect mode, and it shows that the two previous topological defect modes are indeed formed by the edge waveguides, as is shown in Fig. 6(c). For the kink structure with 19 waveguides, the topological defect modes are shown in the middle of the band diagram, and the trivial defect modes (binding modes) shown by the red and green dots, as shown in Fig. 6(b). By computing the eigenvector corresponding to topological defect modes, the field distribution of the topological defect modes of the corresponding color can be obtained. For the antikink structure with 19 waveguides, we can see that in the three topological defect corresponding field distributions, the phenomenon of edge local and central symmetry appears, consistent to the characteristics of topological edge states, as shown in Fig. 6(d). For the kink structure with 19 waveguides, the odd symmetric distribution appears for the field corresponding to the topological defect mode, For the two modes outside of the topological defect mode, the field distribution also shows a local distribution situation, as shown in Fig. 6(e). For the antikink structure with 17 waveguides, the interface mode exhibits a central even symmetry, as is shown in Fig. 6(f). The above theoretical analysis shows that the structure is topologically protected. Detailed description about topological defect modes with respect to the number of waveguide array can be found in Supplementary material [46].

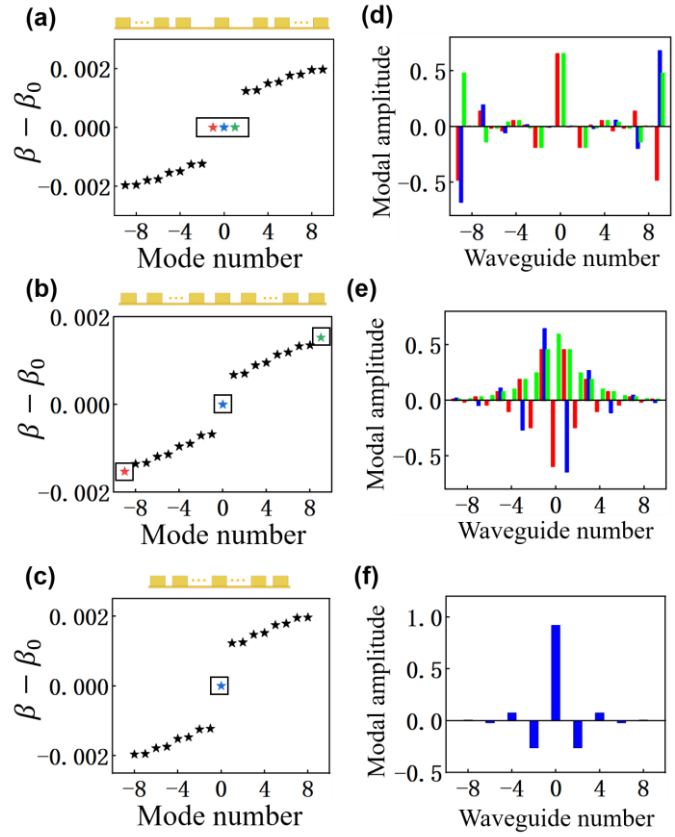

Fig. 6. (a) Mode diagrams of the topologically-protected edge states framed by the box for the antikink structure with 19 waveguides, where three different topological defect modes appear in the center of the energy band, where β_0 represents the propagation constant of the A center waveguide. (b) Mode diagrams with topological defect modes and binding modes framed by the boxes for the kink structure with 19 waveguides, where the topological defect modes appear in the center of the band map, and two trivial bound modes appear at both ends of the energy band. (c) Mode diagrams with topological defect modes framed by the boxes for the antikink structure with 17 waveguides, where only one of the topological defect mode appears at the center of the band gap. (d-f) Field distributions of the topological defect modes and binding modes in Figure (a-c), showing different properties.

To validate the transport properties of the kink and antikink structures in the THz domino waveguide array, we perform a simulation analysis of both structures by using a 3D commercial FEM solution (Comsol Multiphysics 5.6). We set the metal-column as perfect electrical conductors. In the simulation, a linearly polarized THz wave with its polarization direction parallel to the *x*-axis is focused from the bottom side of the sample to the hole array in the *z*-direction. The electric field distribution at 100 μm on the surface of the sample. The energy distribution of the antikink and kink structures observed at 0.5 THz are shown in Fig. 7(a) and 7(c). For the antikink structure, the propagation simulation shows a topological defect that propagates in the structure while always being exponentially localized around the defect. Due to the energy coupling between the adjacent waveguides, a part of the energy is

Authorized licensed use limited to: University of Shanghai For Science and Technology. Downloaded on May 21,2023 at 03:15:13 UTC from IEEE Xplore. Restrictions apply.
© 2023 IEEE. Personal use is permitted, but republication/redistribution requires IEEE permission. See https://www.ieee.org/publications/rights/index.html for more information.

This article has been accepted for publication in IEEE Transactions on Terahertz Science and Technology. This is the author's version which has not been fully edited and content may change prior to final publication. Citation information: DOI 10.1109/TTHZ.2023.3275270

coupled to the upper and lower waveguide, but most of the energy is still localized on the central waveguide. The amplitude distribution at the output port of the antikink structure is shown in Fig. 7(b). It can be seen that most of the energy is localized at the central waveguide. The amplitude with loss of metal is 0.48, indicating the power propagation loss is 0.64 dB/mm. For the kink structure, two binding modes were excited, which are located outside the body band of the band structure, and both have a strong distribution over the central waveguide. Thus, center waveguide input excites both binding modes. Meanwhile, due to their different mode constants, the THz domino plasmon transmission presents a beating effect. The amplitude distribution at the output port of the kink structure is shown in Fig. 7(d). Since the electric field fluctuates between right to the two subcentral waveguides, most of the energy is localized in these two waveguides. The amplitude with loss of metal is 0.36/0.32, indicating the power propagation loss is 0.89 /0.99 dB/mm. The electric field distributions of these two structures correspond exactly to the theoretical analysis [Fig. 6(a-b)]. To highlight the topological transport behavior of the antikink and kink structures, we designed equidistantly spaced ($d_1 = d_2 = 100$ μm) waveguide structures for contrast. The structure without introducing a topology belongs to the defectless structures. It is found that the electric field transport throughout the waveguide and presents an irregular distribution, as shown in Fig. 7(e). The corresponding output port amplitude distribution is shown in Fig. 7(f). The amplitude with loss of metal is 0.2, indicating the power propagation loss is 1.4 dB/mm.

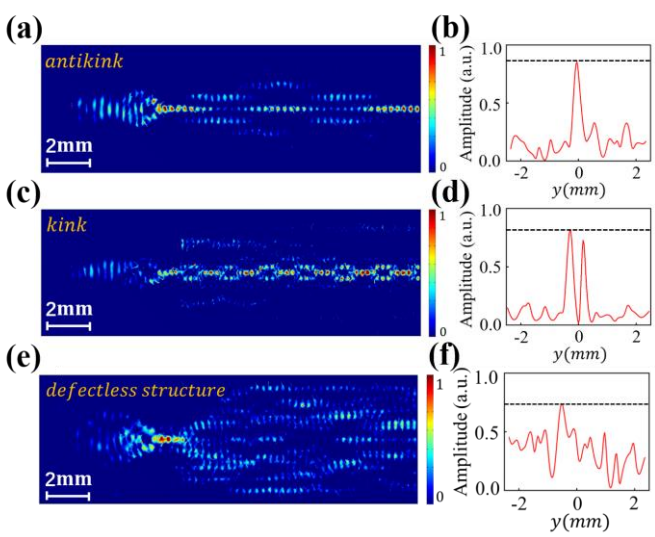

Fig. 7. 3D simulation results at the 0.5 THz frequency. (a) The electric field distributions corresponding to the antikink structure. (b) The amplitude distribution of the output port for the antikink structure. (c) The electric field distributions corresponding to the kink structure. (d) The amplitude distribution of the output port for the kink structure. (e) The electric field distributions corresponding to the defectless structure. (f) The amplitude distribution of the output port for the defectless structure.

IV. THE ROBUSTNESS OF THE TOPOLOGICAL STRUCTURE

a) The antikink structure

To verify the robustness of the topology, structural deviation degree φ is introduced in the waveguide spacing d_1. Change d_1 can directly change the coupling coefficients between the waveguides. For both structures, we introduce different φ by changing d_1. For the antikink structure, most energy remains confined to the central waveguide when introduced 5% and 10% structural deviation degree, which shows good robustness, as is shown in Fig. 8(a) and 8(c). When 15% of the φ is introduced, most energy is still limited to the central waveguide, although the subcentral waveguide also has a partial energy output [Fig. 8(e)]. The amplitude distribution of the output port corresponding to the simulation results under these three different φ are shown in Fig. 8(b) and 8(d) and 8(f). For antikink structures, it is well robust to structural deviation and fits with topological features. The amplitude with loss of metal for φ of 5%,10%,15% is 0.42, 0.38, 0.32, indicating the power propagation loss is 0.75 dB/mm, 0.84 dB/mm, 0.99 dB/mm, respectively. The robustness of the antikink structure with respect to dimer number N can also be found in Supplementary material [46].

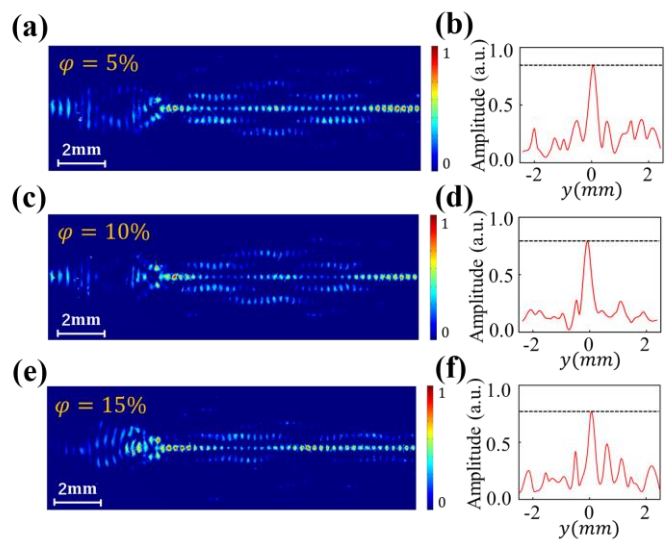

Fig. 8. For the antikink structure, the 3D simulation results with different structural deviation degree φ are introduced at 0.5 THz frequency. (a) The electric field distributions under the 5% deviation degree. (b) The amplitude distribution of the output for 5% deviation degree. (c) The electric field distributions under the 10% deviation degree. (d) The amplitude distribution of the output port for the 10% deviation degree. (e) The electric field distributions under the 15% deviation degree. (f) The amplitude distribution of the output port for the 15% deviation degree.

b) The kink structure

For the kink structure, we verify its robustness in the same way, as shown in Fig. 9. By introducing different structural deviation degree φ on the basis of this structure, we can find that the energy still oscillates around the central waveguide from the normalized electric field distribution of the simulation,

Authorized licensed use limited to: University of Shanghai For Science and Technology. Downloaded on May 21,2023 at 03:15:13 UTC from IEEE Xplore. Restrictions apply.
© 2023 IEEE. Personal use is permitted, but republication/redistribution requires IEEE permission. See https://www.ieee.org/publications/rights/index.html for more information.

This article has been accepted for publication in IEEE Transactions on Terahertz Science and Technology. This is the author's version which has not been fully edited and content may change prior to final publication. Citation information: DOI 10.1109/TTHZ.2023.3275270

but some of the energy is coupled to other waveguides. From the normalized electric field distribution of the output port, it can be seen that after the introduction of different structural deviation degree φ, the energy distribution in the whole waveguide is not obvious, although the sub-central waveguide has two higher peaks. It can be found that the robustness decreases with the increase of φ. Because in kink structure, only two binding modes are excited, which are not in the band gap, they do not have good robustness. This is completely consistent with the theoretical analysis. The amplitude with loss of metal for φ of 5%,10%,15% is 0.3/0.26, 0.28/0.24, 0.22/0.18, indicating the power propagation loss is 1.05/1.17 dB/mm, 1.11/1.24 dB/mm, 1.32/1.49 dB/mm, respectively.

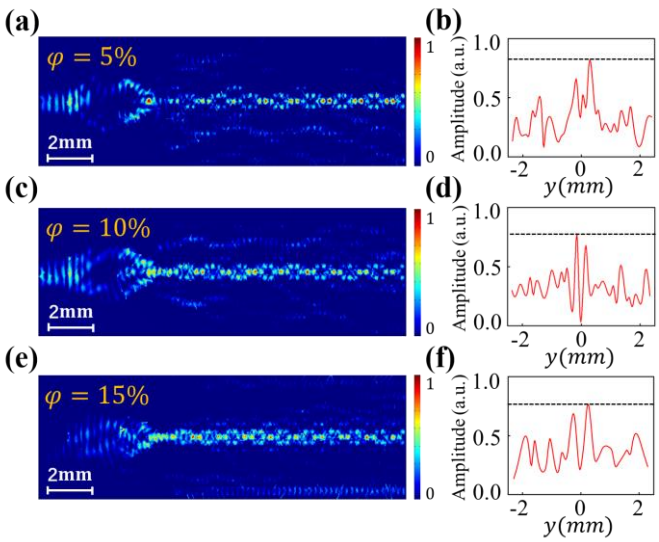

Fig. 9. For the kink structure, 3D simulation results with different structural deviation degree φ are introduced at 0.5 THz frequency. (a) The electric field distributions under the 5% deviation degree. (b) The amplitude distribution of the output port for the 5% deviation degree. (c) The electric field distributions under the 10% deviation degree. (d) The amplitude distribution of the output port for the 10% deviation degree. (e) The electric field distributions under the 15% deviation degree. (f) The amplitude distribution of the output port for the 15% deviation degree.

To demonstrate the robustness of waveguiding by a single topological defect in such domino waveguide platform, we give the fluctuation for *x* and *y* directions for the central waveguide and evaluate the performance improved by introducing the periodic structures. Firstly, the propagation performance was studied by adding the curving central waveguide in the antikink structure (Fig. 10 (a)), which means the inter- and intra-dimer coupling coefficient is not equal at the interface between red dimer chain and blue dimer chain. Simulation result shows that the electric field energy is still found in the center waveguide without dramatically degrading the signal integrity because the structure is still topologically protected, as shown in Fig. 10 (a) and (b). Secondly, we gave the fluctuation for *x* directions for the central waveguide, which is achieved by extracting some pillars in the central domino waveguide and arrange some pillars to randomly deviate from center line. We compared the transmission performances of topological waveguide to single-row domino guide by introducing same defects, as shown in Fig. 10 (c) and (e). The results show that the THz wave can successfully propagate to the end of central waveguide by exciting antikink mode (Fig. 10 (d)), while the energy with domino plasmonic mode in single row guide is reduced significantly, as shown in Fig. 10 (f) and (g).

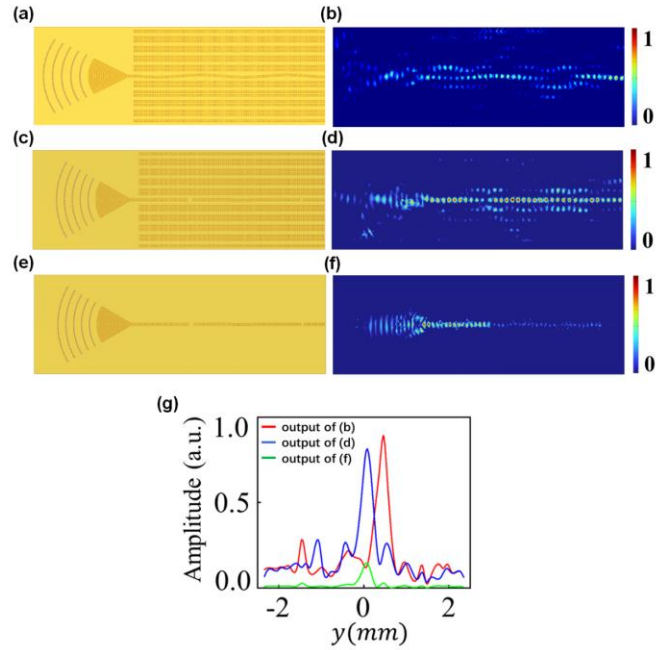

Fig. 10 (a) Schematic of antikink structure with central curving waveguide. (b) The electric field distributions of (a). (c) Schematic of the antikink structure by extracting some pillars in the central domino waveguide and arrange some pillars to randomly deviate from center line. (d) The electric field distributions of (c). (e) Schematic of the single domino waveguide by introducing same defects as (c). (f) The electric field distributions of (e). (g) Amplitude of the electric field of the output ports in (b) (d) (f).

All the above results in an unambiguous way proved the robustness of the system by a single topological defect in a domino waveguide platform.

V. Experiment

A two-step process is employed to fabricate high-quality domino array structure. First, optical lithography and deep reactive ion etching techniques are used to obtain the basic waveguide structure on a 4-inch silicon wafer, where the excitation area is etched into a through-hole. In the second process, a 200-nm-thick gold film metallization of the chips is then conducted in a gold sputter coater. The thickness of gold is selected based on the penetration depth of the THz wave in the metal.

Authorized licensed use limited to: University of Shanghai For Science and Technology. Downloaded on May 21,2023 at 03:15:13 UTC from IEEE Xplore. Restrictions apply.
© 2023 IEEE. Personal use is permitted, but republication/redistribution requires IEEE permission. See https://www.ieee.org/publications/rights/index.html for more information.

This article has been accepted for publication in IEEE Transactions on Terahertz Science and Technology. This is the author's version which has not been fully edited and content may change prior to final publication. Citation information: DOI 10.1109/TTHZ.2023.3275270

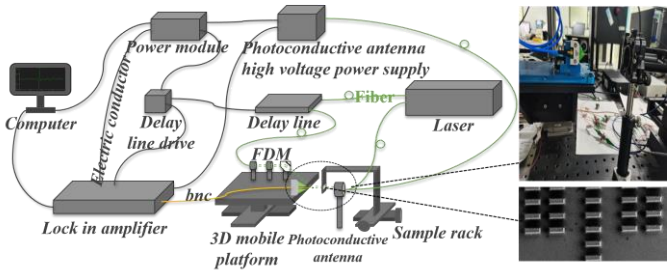

Fig. 11. Illustration of experimental setup. The upper right inset is the experiment process. The lower right inset is the SEM image of the energy transmission region.

We experimentally verify this phenomenon by scanning near-field terahertz microscopy, which has been used in our lab for near field detection of THz functional devices [47-49]. The schematic of the system is shown in Fig. 11. The light source is a femtosecond fiber laser with a central wavelength of 1560 nm. The laser output port is divided into two beams, detection light and pump light. The beam used for detection passes through the optical fiber and radiates the laser through the frequency doubling module to the metal junction of the microprobe. The probe is based on GaAs grown at low temperatures. Since the laser at the wavelength of 1560 nm cannot excite the carrier in GaAs, it is necessary to convert it from 1560 nm to 780 nm. The pump light is connected to the photoconductive emission antenna through the optical fiber delay line, which is two parallel metal wires embedded on the surface of the semiconductor substrate material. Then the photoconductive emission antenna is exposed to the pump light, producing THz radiation. The domino plasmon is generated after the THz wave is input the excitation region of the sample. Since the boundary surface of the waveguide is an evanescent field, the probe needs to be so close to the sample. Then move the probe in the *x*-*y* direction for point-by-point scanning. The probe sends the acquired time-domain signal to the computer by using the current signal amplifier and the phase-lock amplifier, then obtaining the near-field image by the commercial software MATLAB.

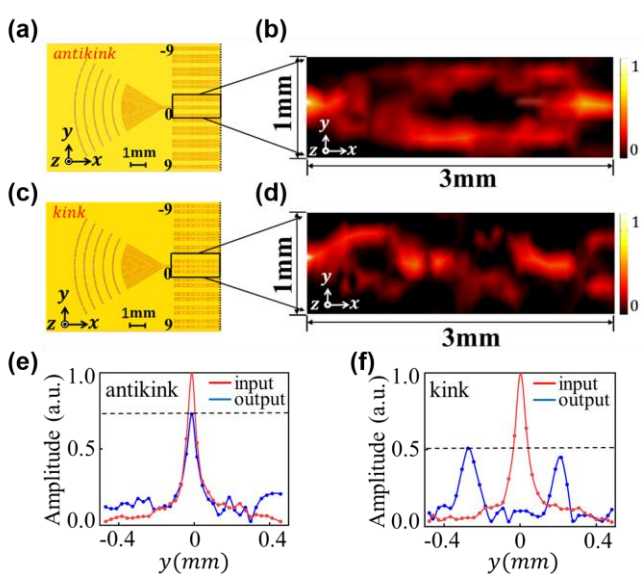

Fig. 12. Experimental results. (a) Schematic representation of the antikink structure. (b) The electric field distributions of the boxed sections in Fig (a). (c) Schematic representation of the kink structure. (d) The electric field distributions of the boxed sections in Fig (c). (e) The amplitude distributions at the output port of the antikink structure in Fig (b). (f) The amplitude distributions at the output port of the kink structure in Fig (d). All the propagation length is 3 mm.

We placed the sample vertically on the sample holder and used the CCD camera to observe the distance between the probe and the sample. We controlled the distance about 100 μm between the probe and the sample. The probe is mounted on a two-dimensional translation detector and moved in the *x*-directions in 100 μm steps and *y*-directions in 30 μm steps [48]. For the actual scanning region of our system, we chose a range of 3×1 mm for scanning. For the antikink structure, the scan range is shown in the boxed area of Fig. 12(a). The scan results indicate that the energy is mostly concentrated in the central waveguide. When transmitting about a third of the distance, the energy moves to the upper and lower waveguide. Despite the energy transition to the upper and lower waveguide, it returns to the central waveguide when transmitting two-thirds of the distance, as shown in Fig. 12(b). This transmission mode is achieved because the energy is input from the waveguide at the center of the interface, which successfully matches the topological defect mode. The topological defect mode is topologically protected, thus enabling robust transmission at the center.

To more precisely observe the amplitude distribution at the output port of the antikink structure, we plotted the amplitude distribution of the input and output ports of the waveguide arrays, as shown in Fig. 12(e). Here we normalized input THz wave instead of output THz wave. The power propagation loss of the antikink structure is 0.91 dB/mm. It can be found that a significant peak appears at the central position, while the energy distribution at other positions is significantly low. The experimental results are perfectly consistent with the simulated results.

For the kink structure, the scan range is shown in the boxed in Fig. 12(c). The scan results indicate that no energy is distributed at the central waveguide when the energy fluctuates to the upper and lower waveguide, as shown in Fig. 12(d). In our experiments, the energy oscillates three times and outputs at the port in the form of oscillation. Through the above topological analysis, the energy of the subcentral waveguide belongs to the two binding modes in the band diagram. They are located outside the body band of the band structure. Thus, a single waveguide input at the center will excite both binding modes simultaneously, and the electric field transport presents a beat effect due to their different mode constants.

To precisely observe the amplitude distribution at the output port of the kink structure, we also plotted the amplitude distribution of the input and output ports of the waveguide arrays, as shown in Fig. 12(f), the power propagation loss of the kink structure is 1.93 dB/mm (left peak) and 2.31 dB/mm (right peak). Two distinct peaks can be found approximately 0.4 mm away from the central waveguide. The position where the central waveguide is located has a very low energy. The experimental results are perfectly consistent with the simulated

Authorized licensed use limited to: University of Shanghai For Science and Technology. Downloaded on May 21,2023 at 03:15:13 UTC from IEEE Xplore. Restrictions apply.
© 2023 IEEE. Personal use is permitted, but republication/redistribution requires IEEE permission. See https://www.ieee.org/publications/rights/index.html for more information.

This article has been accepted for publication in IEEE Transactions on Terahertz Science and Technology. This is the author's version which has not been fully edited and content may change prior to final publication. Citation information: DOI 10.1109/TTHZ.2023.3275270

results.

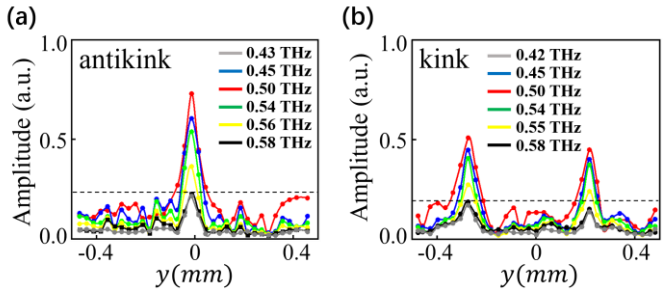

Fig.13 Measured amplitude of the electric field at the output ports of (a) the antikink structure and (b) the kink structure by extracting corresponding frequency.

We also analyzed the amplitude of the electric field at the output port of the antikink and kink structures when propagation length is 3mm by extracting corresponding frequency. The results are shown in Fig. 13. The dynamic range of output amplitude is beyond 0.2-0.73 for antikink structure and 0.2-0.52 for kink structure. The operation bandwidth of the antikink structure is about 150 GHz (0.43-0.58 THz) in the dynamic range and the operation bandwidth of the kink structure is about 160 GHz (0.42-0.58 THz), as shown in Fig. 13 (a) and (b), respectively.

VI. Conclusion

In summary, we realized the THz topologically-protected edge states and binding states by constructing both the kink and antikink structures in the THz domino waveguides array. We analyzed the dispersion and coupling properties of waveguides by supermode theory. Through theoretical analysis, the THz topological defect mode appears at the center of the energy band, and the central transmission of the topological defect mode in the waveguide array is also observed from the simulation results. To verify the robustness of this topology, we perform a simulation analysis by introducing different structural deviation degree, which show that the antikink structures are competent to against the structural deviation. Experimental results verified such topological phase features. Our work introduces topological photonics into THz spectral with domino waveguides array platform. On one side, this platform and its near field measurements can easily demonstrate many quantum phenomena which are found firstly in the condensed matters. On the other side, THz signals manipulated in circuits maintain much more integrity and robustness with fabrication imperfect, sample defects or period disorders by introducing topological protection state.

References

[1] Sirtori, Carlo, "Bridge for the terahertz gap," Nature, vol. 471, no. 6885, pp.132-133, 2002.
[2] Ferguson B, Zhang X C, "Materials for terahertz science and technology," Nature materials, vol. 1, no.1, pp. 26-33, 2002.
[3] Mittleman, Daniel M, "Perspective: Terahertz science and technology," Journal of Applied Physics, vol. 122, no. 23, pp.230901, 2017.
[4] Shen Y C, Lo T, Taday P F, et al, "Detection and identification of explosives using terahertz pulsed spectroscopic imaging," Applied physics letters, vol. 86, no. 24, pp. 241116, 2005.
[5] Xu F, Duan Mu Q D, Li L J, et al, "Nondestructive evaluation of rubber composites using terahertz time domain spectroscopy," Fibres & Textiles in Eastern Europe, 2018.
[6] Nagatsuma T, Ducournau G, Renaud C C, "Advances in terahertz communications accelerated by photonics," Nature Photonics, vol. 10, no. 6, pp. 371-379, 2016.
[7] Chen L, Gao C, Xu J, et al, "Observation of electromagnetically induced transparency-like transmission in terahertz asymmetric waveguide-cavities systems," Optics letters, vol. 38, no. 9, pp. 1379-1381, 2013.
[8] Chen L, Ge Y, Zang X, et al, "Tunable phase transition via radiative loss controlling in a terahertz attenuated total reflection-based metasurface," IEEE Transactions on Terahertz Science and Technology, vol. 9, no. 6, pp. 643-650, 2019.
[9] Chen L, Zhu Y, Zang X, et al, "Mode splitting transmission effect of surface wave excitation through a metal hole array," Light: Science & Applications, vol. 2, no. 3, pp. e60, 2013.
[10] Lv B, Ouyang C, Zhang H, et al, "All-dielectric metasurface-based quad-beam splitter in the terahertz regime," IEEE Photonics Journal, vol. 12, no. 5, pp. 1-10, 2020.
[11] Cheng Q, Wang J, Ma L, et al, "Achromatic terahertz Airy beam generation with dielectric metasurfaces," Nanophotonics, vol. 10, no. 3, pp. 1123-1131, 2021.
[12] Xi K, Fang B, Ding L, et al, "Terahertz Airy beam generated by Pancharatnam-Berry phases in guided wave-driven metasurfaces," Optics Express, vol. 30, no. 10, pp. 16699-16711, 2022.
[13] Kumar A, Gupta M, Pitchappa P, et al, "Phototunable chip-scale topological photonics: 160 Gbps waveguide and demultiplexer for THz 6G communication," Nature communications, vol. 13, no. 1 pp. 1-9, 2022.
[14] Kumar A, Gupta M, Pitchappa P, et al, "Active Ultrahigh-Q (0.2× 106) THz Topological Cavities on a Chip," Advanced Materials, pp. 2202370, 2022.
[15] Kumar A, Gupta M, Singh R, "Topological integrated circuits for 5G and 6G," Nature Electronics, vol. 5, no. 5, pp. 261-262, 2022.
[16] Chen L, Liao D, Guo X, et al, "Terahertz time-domain spectroscopy and micro-cavity components for probing samples: a review," Frontiers of Information Technology & Electronic Engineering, vol. 20, no. 5, pp. 591-607, 2019.
[17] Zhou J, Chen L, Sun Q, et al, "Terahertz on-chip sensing by exciting higher radial order spoof localized surface plasmons," Applied Physics Express, vol. 13, no. 1, pp. 012014, 2019.
[18] Tsuruda K, Ishigaki T, Suminokura A, et al, "Ultralow-loss photonic-crystal waveguides for gigabit terahertz-wave communications," IEEE International Topical Meeting on Microwave Photonics (MWP). IEEE, pp. 9-12, 2013.
[19] Tsuruda K, Fujita M, Nagatsuma T, "Extremely low-loss terahertz waveguide based on silicon photonic-crystal slab," Optics express, vol. 23, no. 25, pp. 31977-31990, 2015.
[20] Withayachumnankul W, Fujita M, Nagatsuma T, "Integrated silicon photonic crystals toward terahertz communications," Advanced Optical Materials, vol. 6, no. 16, pp. 1800401, 2018.
[21] Withayachumnankul W, Yamada R, Fujita M, et al, "All-dielectric rod antenna array for terahertz communications" APL Photonics, vol. 3, no. 5, pp. 051707, 2018.
[22] Gao W, Yu X, Fujita M, et al, "Effective-medium-cladded dielectric waveguides for terahertz waves" Optics express, vol. 27, no. 26, pp. 38721-38734, 2019.
[23] Headland D, Withayachumnankul W, Yu X, et al, "Unclad microphotonics for terahertz waveguides and systems" Journal of Lightwave technology, vol. 38, no. 24, pp. 6853-6862, 2020.
[24] Verstuyft M, Akiki E, Vanwolleghem M, et al, "Short bends using curved mirrors in silicon waveguides for terahertz waves" Optics Express, vol. 30, no. 5, pp. 6656-6670, 2022.
[25] Koala, Ratmalgre, et al, "Ultra-Low-Loss and Broadband All-Silicon Dielectric Waveguides for WR-1 Band (0.75–1.1 THz) Modules" Photonics, vol. 9, no. 8, pp. 515, 2022.
[26] Rivera-Lavado A, Ali M, Gallego-Cabo D, et al, "Contactless RF probe interconnect technology enabling broadband testing to the terahertz range" IEEE Transactions on Terahertz Science and Technology, vol. 13, no. 1, pp. 34-43, 2022.
[27] Yang Y, Yamagami Y, Yu X, et al, "Terahertz topological photonics for on-chip communication," Nature Photonics, vol. 14, no. 7, pp. 446-451, 2020.
[28] The user guide manual in: www.mtinstruments.com
[29] Martín-Cano D, Nesterov M L, Fernandez-Dominguez A I, et al,

Authorized licensed use limited to: University of Shanghai For Science and Technology. Downloaded on May 21,2023 at 03:15:13 UTC from IEEE Xplore. Restrictions apply.
© 2023 IEEE. Personal use is permitted, but republication/redistribution requires IEEE permission. See https://www.ieee.org/publications/rights/index.html for more information.

This article has been accepted for publication in IEEE Transactions on Terahertz Science and Technology. This is the author's version which has not been fully edited and content may change prior to final publication. Citation information: DOI 10.1109/TTHZ.2023.3275270

"Domino plasmons for subwavelength terahertz circuitry," Optics Express, vol. 18, no. 2, pp. 754-764, 2010.

[30] Zhang Y, Xu Y, Tian C, et al, "Terahertz spoof surface-plasmon-polariton subwavelength waveguide," Photonics Research, vol. 6, no. 1, pp. 18-23, 2018.

[31] Yuan M, Lu Y, Zhang Y, et al, "Curved terahertz surface plasmonic waveguide devices," Optics Express, vol. 28, no. 2, pp. 1987-1998, 2020.

[32] Zhang Y, Lu Y, Yuan M, et al, "Rotated Pillars for Functional Integrated On-Chip Terahertz Spoof Surface-Plasmon-Polariton Devices," Advanced Optical Materials, pp. 2102561, 2022.

[33] Yuan M, Wang Q, Li Y, et al, "Ultra-compact terahertz plasmonic wavelength diplexer," Applied Optics, vol. 59, no. 33, pp. 10451-10456, 2020.

[34] Yuan M, Wang Q, Li Y, et al, "Terahertz spoof surface plasmonic logic gates," Iscience, vol. 23, no. 11, pp. 101685, 2020.

[35] Cheng Q, Chen T, Yu D, et al, "Flexibly designed spoof surface plasmon waveguide array for topological zero-mode realization," Optics Express, vol. 26, no. 24, pp. 31636-31647, 2018.

[36] Chen T, Yu Y, Song Y, et al, "Distinguishing the topological zero mode and Tamm mode in a microwave waveguide array," Annalen der Physik, vol. 531, no. 12, pp. 1900347, 2019.

[37] Song W, Sun W, Chen C, et al, "Breakup and recovery of topological zero modes in finite non-Hermitian optical lattices," Physical review letters, vol. 123, no. 16, pp. 165701, 2019.

[38] Song W, Sun W, Chen C, et al, "Robust and broadband optical coupling by topological waveguide arrays," Laser & Photonics Reviews, vol. 14, no. 2, pp. 1900193, 2020.

[39] Heeger A J, Kivelson S, Schrieffer J R, et al, "Solitons in conducting polymers," Reviews of Modern Physics, vol. 60, no. 3, pp. 781, 1988.

[40] Shen X, Jun Cui T, "Planar plasmonic metamaterial on a thin film with nearly zero thickness," Applied physics letters, vol. 102, no. 21, pp. 211909, 2013.

[41] Zhang X, Xu Q, Xia L, et al, "Terahertz surface plasmonic waves: a review," Advanced Photonics, vol. 2, no. 1, pp. 014001, 2020.

[42] Yuan M, Li Y, Lu Y, et al, "High-performance and compact broadband terahertz plasmonic waveguide intersection," Nanophotonics, vol. 8, no. 10, pp. 1811-1819, 2019.

[43] Chen L, Xu N, Singh L, et al, "Defect-induced Fano resonances in corrugated plasmonic metamaterials," Advanced Optical Materials, vol. 5, no. 8, pp. 1600960, 2017.

[44] Maier S A, "Plasmonics: fundamentals and applications," New York: springer, 2007.

[45] Ebbesen T W, Lezec H J, Ghaemi H F, et al, "Extraordinary optical transmission through sub-wavelength hole arrays," Nature, vol. 391, no. 6668, pp. 667-669, 1998.

[46] See Supplemental Material for a detailed description of bends and passive routing structures, the SSH model for the domino waveguide dimer chains in one dimension, the robustness of the antikink structure with respect to dimer number N, the number of waveguide array, the role of periodic structure for propagation x-direction, performances of various THz waveguides, and Supplemental Figures.

[47] Zang X F, Gong H H, Li Z, et al, "Metasurface for multi-channel terahertz beam splitters and polarization rotators," Applied Physics Letters, vol. 112, no. 17, pp. 171111, 2018.

[48] Zang X F, Zhu Y M, Mao C X, et al, "Manipulating terahertz plasmonic vortex based on geometric and dynamic phase," Advanced Optical Materials, vol. 7, no. 3, pp. 1801328, 2019.

[49] Yao B, Zang X, Li Z, et al, "Dual-layered metasurfaces for asymmetric focusing," Photonics Research, vol. 8, no. 6, pp. 830-843, 2020.

Pan Hu is currently working toward the M.S. degree in electronic information with University of Shanghai for Science and Technology, Shanghai,China.

His research interests is in Terahertz Silicon Photonic Devices, Plasmonics, and Topological Photonics.

Lin Chen received the B.S. and M.S. degrees in electrical engineering from Southeast University, Jiangsu, China, in 2002 and 2005, respectively, and the Ph.D. degree in optics from Shanghai Jiao Tong University, Shanghai, China, in 2008. From 2007 to 2008, he was with Avanex Corporation as Senior Engineer. From 2012 to 2013, he was a Visiting Scholar with the State Key Laboratory of Millimeter Waves, Southeast University. From 2015 to 2016, He was a Visiting Researcher with Ultrafast THz Optoelectronic Laboratory, Oklahoma State University, Stillwater, OK, USA.

He was designated Shanghai "Dawn scholar", "Chengguang scholar", "Top-Notch Young Talents", "Rising-Star", "Pujiang talent" and other talent titles. He was also award Publons Peer Review Award (2018 and 2019). As the first person in charge, he has undertaken a number of national level projects, including the national key R&D plan "major scientific instrument and equipment development" (chief scientist), two national major instrument projects (project), National Natural Foundation of China (general & Youth) and several projects in Shanghai.

At present, He has published more than 70 peer reviewed papers with more than 2000 citations and H-index 26 (including 4 Highly Cited Paper) in Science Citation Indexed journal such as Light: Science & Applications, etc. He has also applied for more than 40 invention patents, 21 authorized and 1 US patent.

He is currently the Editorial Board Member of Frontiers in Physics, Guest Editor and Corresponding Expert of Frontiers of Information Technology & Electronic Engineering.

Alexander P. Shkurinov graduated in 1985 from Lomonosov Moscow State University (MSU), Moscow, Russia. He received the Ph.D. degree and Doctor of Physics and Math Sciences from MSU in 1988 and 2013, respectively. Since 2015 he has been a Professor at the Faculty of Physics of Lomonosov Moscow State University. The research interests of Alexander Shkurinov are mainly centered around the development and application of femtosecond laser techniques, time-resolved spectroscopy of molecules in liquid phase, nonlinear optics and THz techniques and spectroscopy. He has authored and coauthored more than 300 papers in peer-reviewed scientific journals, was invited to deliver more than 60 invited lectures and talks. In 2008 the Russian Optical Society awarded Alexander Shkurinov with the Medal in honor of Prof. Rozhdestvensky for his contribution into the development of optical science and technology.

Yiming Zhu graduated from the University of Tokyo with a Ph.D. degree. He is a "Youth Science and technology innovation leader" and "Young Yangtze Professor" in the University of Shanghai for Science and Technology, and currently serves as a vice director of the Shanghai Key Lab of Modern Optical System. He is also the "The national key talent project", "Outstanding Youth Foundation", and "special State Council allowance" winner. His research focuses on terahertz technologies and applications, including terahertz devices, terahertz spectroscopy, imaging systems, terahertz bio-applications, etc. Up to now, he has published more than 100 papers, including >40 papers in Light Sci. & Appl., Adv. Opt. Mater., Appl. Phys. Lett., Opt. Lett., Opt. Exp., et al (Top 5%), including 5 papers are selected as ESI papers. He has been responsible for more than 20 projects at the national and ministerial/provincial levels, which include one project supported by the National 863 Project, 4 projects supported by the National Natural Science Foundation of China, 2 sub-projects supported by the National 973 Project, 2 projects supported by the Major National Development Project of Scientific Instrument and Equipment, etc. In 2012, he won the title of "New Century Talent" from the Ministry of Education. In 2013, he

Authorized licensed use limited to: University of Shanghai For Science and Technology. Downloaded on May 21,2023 at 03:15:13 UTC from IEEE Xplore. Restrictions apply.
© 2023 IEEE. Personal use is permitted, but republication/redistribution requires IEEE permission. See https://www.ieee.org/publications/rights/index.html for more information.

This article has been accepted for publication in IEEE Transactions on Terahertz Science and Technology. This is the author's version which has not been fully edited and content may change prior to final publication. Citation information: DOI 10.1109/TTHZ.2023.3275270

was appointed as a council member of the China Instrument and Control Society. In 2014, he won the title of “excellent academic leaders of Shanghai”, and was appointed as a council member of the China Optical Engineering Society and a member of the China Youth Scientist and Technician Association. In 2016, he was selected as “Shanghai leading talent” and “Young Yangtze Scholar”. In 2017, he was awarded the “Outstanding Youth Foundation” by the “National Natural Science Foundation of China”, and selected into “The national key talent project”. In 2018, he was recognized as a “Youth Science and technology innovation leader” by the “Ministry of Science and Technology of China”, and received the special State Council allowance. Furthermore, he also won the first prize of Shanghai Teaching Achievement Award. He is currently the director of the Terahertz Spectral and Imaging Technology National Cooperative Innovation Center, the Terahertz Precision Biomedical Technology Overseas Expertise Introduction Center for Discipline Innovation, the Terahertz Technology Innovation International Joint Laboratory at University of Shanghai for Science and Technology and Lomonosov Moscow State University.

Songlin Zhuang graduated from Physics Department of Fudan University in 1962. From 1962 to 1979, he worked in Shanghai Institute of Optical Instruments. In 1979, he went to Michigan State University (USA) for visiting research, and in 1982 he obtained his doctorate in the Department of Electronic Engineering of Pennsylvania State University (USA). In 1983, he returned to Shanghai Institute of Optical Instruments as director and senior engineer. From 1988 to 1992, he served as director and researcher of Shanghai Institute of Laser Technology. Since 1995, he has been the president of School of OptIcal-Electronic and Computer Engineering, University of Shanghai for Science and Technology.

He has won many ministerial level science and technology progress awards and many honorary awards. More than 100 kinds of optical systems and instruments have been designed. He is the first researcher to carry out optical system CAD in China. He presided over and completed the largest optical instrument design software system in China, and made original achievements in the optimization method of statistical test total extreme value and the nonlinear model of tolerance. In the field of optical image psychophysics experiment, he has carried out the first work in China. He has made a comprehensive and systematic research on incoherent optical information processing and rainbow holography, and is known as "one of the main contributors of modern white light information processing". A variety of optical methods have been proposed in the study of phase recovery of complex objects, which has opened up a new research direction in this field. The CdSe liquid crystal light valve has reached the international advanced level at that time. Outstanding achievements have been made in super-resolution optical imaging, grating diffraction vector mode theory, high-speed optical multi-channel mode / number transformation, transformation optics and artificial medium materials. Over the years, he has personally supervised more than 20 master's and doctoral students. The graduates have made a lot of contributions in the field of optical engineering at home and abroad. One of his students' doctoral dissertation was selected as the National 100 Excellent Doctoral Dissertations in 2009. The course of optical information technology that he taught has won the National Excellent Course in 2008.

Authorized licensed use limited to: University of Shanghai For Science and Technology. Downloaded on May 21,2023 at 03:15:13 UTC from IEEE Xplore. Restrictions apply.
© 2023 IEEE. Personal use is permitted, but republication/redistribution requires IEEE permission. See https://www.ieee.org/publications/rights/index.html for more information.